Image degradation due to surface scatter in the presence of aberrations

Narak Choi and James E. Harvey*

The Center for Research and Education in Optics and Lasers (CREOL), The University of Central Florida, Orlando, Florida 32816, USA

*Corresponding author: harvey@creol.ucf.edu

Received 1 August 2011; revised 3 October 2011; accepted 7 October 2011; posted 24 October 2011 (Doc. ID 151993); published 3 February 2012

Image analysis in the presence of surface scatter due to residual optical fabrication errors is often perceived to be complicated, nonintuitive, and achieved only by computationally intensive nonsequential ray tracing with commercial optical analysis codes such as ASAP, Zemax, Code V, TracePro, or FRED. However, we show that surface scatter can be treated very similarly to conventional wavefront aberrations. For multielement imaging systems degraded by both surface scatter and aberrations, the composite point spread function is obtained in explicit analytic form in terms of convolutions of the geometrical point spread function and scaled bidirectional scattering distribution functions of the individual surfaces of the imaging system. The approximations and assumptions in this formulation are discussed, and the result is compared to the irradiance distribution obtained using commercial software for the case of a two-mirror telescope operating at an extreme ultraviolet wavelength. The two results are virtually identical.

OCIS codes: 110.2960, 080.1005, 290.5880, 290.1483, 290.5835.

1. Introduction

Image degradation due to conventional aberrations has become well understood over the past century, and surface scatter phenomena has been investigated extensively for the past half century. However, the two image degradation mechanisms are usually treated separately even though they are essentially the same phenomenon, i.e., the deviation of the light from the ideal direction as it propagates through an imaging system.

Recently, Peterson suggested a way of analyzing image degradation due to surface scatter in a multielement system [1,2], and subsequently, Harvey *et al.* extended Peterson's method to the more general case of moderately rough surfaces [3]. However, their analyses are still restricted to paraxial, aberration-free optical systems. In this paper, image degradation, as characterized by the point spread function (PSF) is obtained in explicit analytic form for systems in which both aberrations and surface scatter are dominant image degradation mechanisms.

That this explicit form is expressed as the convolution of the geometrical PSF_G with a scattering PSF_S is convenient; however, the accuracy depends upon the validity of the approximations and assumptions made in the mathematical development. Goodman [4] has shown that a similar linear systems approach to image analysis as degraded by diffraction and geometrical aberrations is not strictly true, and Harvey and Krywonos [5] have quantitatively evaluated the assumption for different amounts of defocus. They then proceed to successfully apply the linear system formulation of image quality to the case of an x-ray telescope [6,7].

This paper confirms that the explicit expression for the system PSF is not rigorously true; however, it discusses the assumptions and approximations made in the mathematical formulation, explains why the explicit expression should be sufficiently accurate for most optical engineering applications, then goes on to numerically validate it for the specific

1559-128X/12/050535-12$15.00/0

application of a two-mirror extreme ultraviolet (EUV) telescope.

For these short-wavelength EUV applications, the effects of aberrations exceed the Rayleigh (diffraction) limit by a substantial factor, and diffraction effects become relatively insignificant [8]. Also at these short wavelengths, scattering effects are drastically increased for a given residual surface roughness. The size of the Airy disk is thus small compared to both the geometrical "spot size" and "scattering effects." We have thus ignored diffraction effects in the analysis presented in this paper and, as the title suggests, discuss image degradation due only to scatter effects in the presence of aberrations.

In Section 2, the PSF of a scatter-free system is reviewed for the purpose of showing the validity of our method of analysis. Then, using the same methodology, the analysis is extended to imaging systems exhibiting both aberrations and surface scatter in Section 3. In Section 4 our results are compared to those obtained using the computationally intensive, nonsequential ray-tracing capabilities of a commercially available optical design and analysis code.

2. Review of Imaging Equations by an Aberrated Optical System

Generally, the impulse response function of a system can be described by the following integral form:

$$\Psi_{\text{output}}(\eta_{\text{output}}) = \int \mathrm{d}\eta_{\text{input}} K(\eta_{\text{output}}, \eta_{\text{input}}) \cdot \Psi_{\text{input}}(\eta_{\text{input}}), \quad (1)$$

where the function K is called the kernel function, which describes the system characteristics [9]. One of the famous impulse response functions is the PSF of optical imaging systems. In geometric optics, the integral form is rarely used for analysis. However, in this paper a new formalism using the form of Eq. (1) is developed in order to describe the geometrical PSF as well as the scattering PSF.

After introducing notations and definitions used in this paper in Subsection 2.A, this fundamental formalism will be validated for a single-surface imaging system in Subsection 2.B, for a two-surface imaging system in Subsection 2.C, and finally, for an n-surface imaging system in Subsection 2.D, before extending this analysis to the case of image degradation due to aberrations and scattered light in Section 3. In the following sections, absorption and vignetting effects are ignored and some parameters are dropped in the kernel function for simplicity.

A. Notations and Definitions

Figure 1 illustrates an optical system consisting of a series of coaxial optical surfaces [10]. The Gaussian image of a point object formed by the first optical surface acts as an object for the second optical surface, and so on. Thus, the image plane of the jth optical surface (referred to as the jth image plane) is the same as the object plane of the $(j+1)$th optical surface [referred to as the $(j+1)$th object plane], the first object plane is the same as the object plane of the total optical system (referred to as object plane), and last image plane is the same as image plane of the total optical system (referred to as image plane). $\mathbf{x}_j = (x_j, y_j)$ is the position where a ray intersects the jth image plane, and $\mathbf{x}_0$ is the position where a ray intersects the object plane. z_j, z'_j are defined as conjugate distances of the jth optical surface divided by the index of refraction of the corresponding space, and the transverse magnification of the jth optical surface is given by $m_j = z'_j/z_j$. Each optical surface may have aberrations, and the primary wave aberration function of the jth optical surface (referred to as the jth wave aberration function) is defined at the exit pupil of the jth optical surface (referred to as the jth exit pupil), and the last exit pupil coincides with the exit pupil of the total optical system (referred to as exit pupil). $\boldsymbol{\xi}_j = (\xi_j, \eta_j)$ is the exit pupil coordinate of a ray in the jth exit pupil, and $m_{j-n}^{(p)}$ denotes the pupil magnification between the jth exit pupil and the nth exit pupil. r_j is defined by the distance from the center of the jth exit pupil to the jth image plane divided by the index of refraction

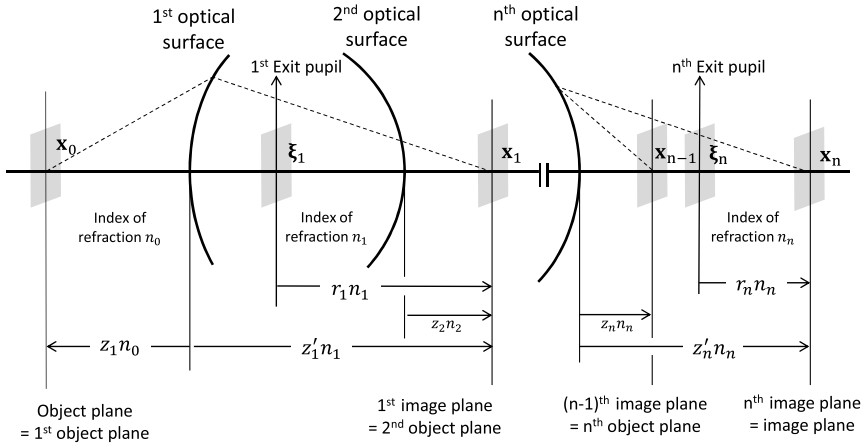

Fig. 1. Schematic layout of an optical imaging system consisting of a series of coaxial optical surfaces.

of the corresponding space. W_j is the jth wave aberration function given by

$$W_j(\boldsymbol{\xi}_j|\mathbf{x}_{j-1}) = W_{040}p_j^2 + W_{131}p_jc_j + W_{222}c_j^2 + W_{220}p_jq_j + W_{311}q_jc_j, \quad (2)$$

where $p_j = \boldsymbol{\xi}_j \cdot \boldsymbol{\xi}_j/a_j^2$, $q_j = \mathbf{x}_{j-1} \cdot \mathbf{x}_{j-1}/b_j^2$, and $c_j = \boldsymbol{\xi}_j \cdot \mathbf{x}_{j-1}/a_jb_j$. a_j is the maximum pupil height in the jth exit pupil, and b_j is the maximum object height in the jth object plane. Note that $b_j = m_1m_2\cdots m_{j-1}b$, where b is the maximum object height in the object plane. If an optical system consists of n elements, the primary aberration function of the total system W is obtained by

$$W(\boldsymbol{\xi}_n|\mathbf{x}_0) = \sum_{j=1}^{n} W_j(\boldsymbol{\xi}_n/m_{j-n}^{(p)}|m_1m_2\cdots m_{j-1}\mathbf{x}_0). \quad (3)$$

The third-order transverse ray aberration function $\boldsymbol{\varepsilon}_j(\boldsymbol{\xi}_j|\mathbf{x}_{j-1})$ is introduced and is defined by

$$\boldsymbol{\varepsilon}_j(\boldsymbol{\xi}_j|\mathbf{x}_{j-1}) = -r_j\nabla_j W_j(\boldsymbol{\xi}_j|\mathbf{x}_{j-1}), \quad (4)$$

which is a ray displacement with respect to Gaussian image position in the jth image plane, and $\nabla_j = (\partial/\partial\xi_j, \partial/\partial\eta_j)$ is the gradient operator. The Lagrange invariant has been used to obtain the third-order transverse ray aberration function of the total n-element optical system:

$$\begin{aligned}\boldsymbol{\varepsilon}(\boldsymbol{\xi}_n|\mathbf{x}_0) &= -r_n\nabla_n W(\boldsymbol{\xi}_n|\mathbf{x}_0)\\ &= -\sum_{j=1}^{n} r_n\nabla_n W_j(\boldsymbol{\xi}_n/m_{j-n}^{(p)}|m_1m_2\cdots m_{j-1}\mathbf{x}_0)\\ &= -\sum_{j=1}^{n}[m_{j+1}\cdots m_n r_j\nabla_j W_j(\boldsymbol{\xi}_j|\mathbf{x}_{j-1})]\\ &= \sum_{j=1}^{n}[m_{j+1}\cdots m_n\boldsymbol{\varepsilon}_j(\boldsymbol{\xi}_j|\mathbf{x}_{j-1})]. \quad (5)\end{aligned}$$

Note that the last exit pupil coincides with the exit pupil of the total optical system.

B. Review of Imaging Equations for a Single Surface

Figure 2 illustrates a single optical surface imaging system. If there is no aberration, the point source position $\mathbf{x}_0$ in the object plane is relocated to $\mathbf{x}_1$ in the image plane by

$$\delta(\mathbf{x}-\mathbf{x}_1) = \delta\left(\mathbf{x} - \frac{z_1'}{z_1}\mathbf{x}_0\right). \quad (6)$$

Strictly speaking, the emittance of a point source cannot be defined. However, by utilizing an infinitesimally small area centered on the point source position, the power emitted from the point source divided by the infinitesimally small area is considered to be the emittance. By defining the object irradiance distribution function for such a point source as $E_0(\mathbf{x}_0) = \delta(\mathbf{x}_0 - \mathbf{x}_{\text{obj}})$, the transferred irradiance can be expressed by

$$\begin{aligned}E(\mathbf{x}_1) &= P_{\text{inc}}\int \mathrm{d}^2\mathbf{x}_0 \frac{1}{z_1'^2}\delta\left(\frac{\mathbf{x}_1}{z_1'} - \frac{\mathbf{x}_0}{z_1}\right)E_0(\mathbf{x}_0)\\ &= P_{\text{inc}}\delta(\mathbf{x}_1 - m_1\mathbf{x}_{\text{obj}}), \quad (7)\end{aligned}$$

where the domain of integration in this paper is $[-\infty, \infty]$ and $d^2\mathbf{x} = dxdy$. P_{inc} is the power collected by the entrance pupil of the system.

If the optical surface has aberrations, the image plane position of a ray passing through $\boldsymbol{\xi}_1$ is given by

$$\delta(\mathbf{x}-\mathbf{x}_1) = \delta\left(\mathbf{x} - \frac{z_1'}{z_1}\mathbf{x}_0 - \boldsymbol{\varepsilon}_1(\boldsymbol{\xi}_1|\mathbf{x}_0)\right). \quad (8)$$

By assuming uniform irradiance E_p in the exit pupil, and assuming that each ray leaving the exit pupil carries equal power, the transferred irradiance of the point source by the aberrated single optical surface is given by

$$\begin{aligned}E(\mathbf{x}_1) = E_p\int \mathrm{d}^2\mathbf{x}_0 \int \mathrm{d}^2\boldsymbol{\xi}_1 \frac{1}{z_1'^2}\delta\left(\frac{\mathbf{x}_1}{z_1'} - \frac{\mathbf{x}_0}{z_1} - \frac{\boldsymbol{\varepsilon}_1(\boldsymbol{\xi}_1|\mathbf{x}_0)}{z_1}\right)\\ \times E_0(\mathbf{x}_0). \quad (9)\end{aligned}$$

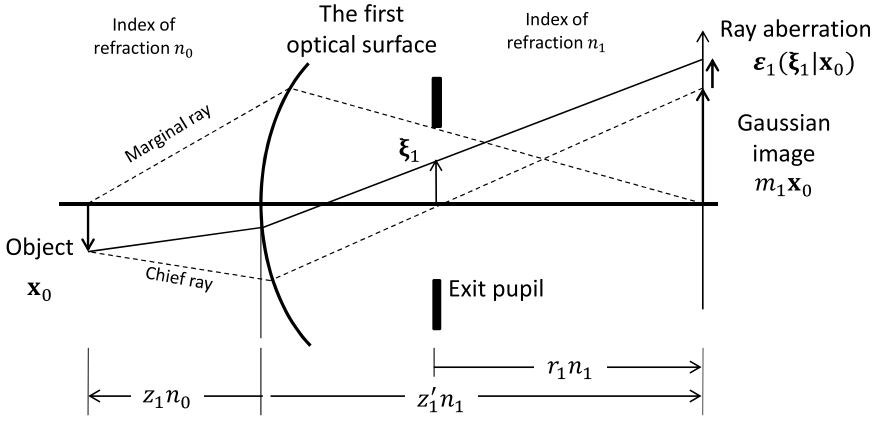

Fig. 2. Schematic layout of a single-surface optical imaging system.

Using the identity

$$\delta\left(\frac{\mathbf{x}}{a}-b+c\right)=\int \mathrm{d}^2\mathbf{x}'\delta\left(\frac{\mathbf{x}'}{a}-b\right)\delta(\mathbf{x}-\mathbf{x}'+ac), \quad (10)$$

Eq. (9) turns into

$$E(\mathbf{x}_1)=\int \mathrm{d}^2\mathbf{x}_1'\left[\frac{1}{z_1'^2}\delta\left(\frac{\mathbf{x}_1'}{z_1'}-\frac{\mathbf{x}_{\mathrm{obj}}}{z_1}\right)\right] \times\left[E_p\int \mathrm{d}^2\xi_1\delta(\mathbf{x}_1-\mathbf{x}_1'-\boldsymbol{\varepsilon}_1(\boldsymbol{\xi}_1|\mathbf{x}_{\mathrm{obj}}))\right]. \quad (11)$$

Comparing Eqs. (8) and (11), the variable $\mathbf{x}_1'$ can be interpreted as the Gaussian image position in the image plane. Equation (11) can be written as

$$E(\mathbf{x}_1)=\mathrm{PSF}_G(\mathbf{x}_1|\mathbf{x}_{\mathrm{obj}})\otimes\delta(\mathbf{x}_1-m_1\mathbf{x}_{\mathrm{obj}}), \quad (12)$$

where $\otimes$ is the symbolic notation for the two-dimensional convolution operation and PSF_G is the geometrical PSF with respect to the Gaussian image point

$$\mathrm{PSF}_G(\mathbf{x}_1|\mathbf{x}_{\mathrm{obj}})\cong E_p\int \mathrm{d}^2\xi_1\delta(\mathbf{x}_1+r_1\nabla_1 W(\boldsymbol{\xi}_1|\mathbf{x}_{\mathrm{obj}})). \quad (13)$$

The validity of expressing the geometrical PSF as Eq. (13) will be discussed in Appendix A.

C. Review of Imaging Equations for Two Surfaces

Figure 3 shows a two-surface optical imaging system. Consider the trajectory of a ray passing P_0, P_1, P_2, and P_4 and assume that the position of the ray in the exit pupil of the second optical surface is $\boldsymbol{\xi}_2$. In the view of the first optical surface, the ray comes from P_0 and is refracted at P_1 and intersects its image plane at P_3. For the second surface, the ray "comes" from the virtual point P_3, is refracted at P_2, and intersects its image plane at P_4. Thus, in the view of the second surface, the position of the point P_4, which is represented by $\mathbf{x}_2(\boldsymbol{\xi}_2)$, can be expressed by

$$\delta(\mathbf{x}-\mathbf{x}_2)=\int \mathrm{d}^2\mathbf{x}_1\delta\left(\mathbf{x}_1-\frac{z_1'}{z_1}\mathbf{x}_0-\boldsymbol{\varepsilon}_1(\boldsymbol{\xi}_1|\mathbf{x}_0)\right) \times\delta\left(\mathbf{x}-\frac{z_2'}{z_2}\mathbf{x}_1-\boldsymbol{\varepsilon}_2(\boldsymbol{\xi}_2|\mathbf{x}_1)\right), \quad (14)$$

where $\boldsymbol{\xi}_1=\boldsymbol{\xi}_2/m_{1\text{–}2}^{(p)}$. However, in third-order aberration theory, the Gaussian reference sphere of the second optical surface centers on P_5, which is the Gaussian image point of P_0 by the first optical surface. And the total ray aberration is obtained by combining $m_2\boldsymbol{\varepsilon}_1(\boldsymbol{\xi}_1|\mathbf{x}_0)$ and $\boldsymbol{\varepsilon}_2(\boldsymbol{\xi}_2|m_1\mathbf{x}_0)$. Thus, $\mathbf{x}_2(\boldsymbol{\xi}_2)$ can be expressed by

$$\delta(\mathbf{x}-\mathbf{x}_2)\cong\int \mathrm{d}^2\mathbf{x}_1\delta\left(\mathbf{x}_1-\frac{z_1'}{z_1}\mathbf{x}_0\right) \times\delta\left(\mathbf{x}-\frac{z_2'}{z_2}\mathbf{x}_1-\frac{z_2'}{z_2}\boldsymbol{\varepsilon}_1(\boldsymbol{\xi}_1|\mathbf{x}_0)-\varepsilon_2\left(\boldsymbol{\xi}_2\middle|\frac{z_1'}{z_1}\mathbf{x}_0\right)\right). \quad (15)$$

Comparing Eqs. (14) and (15) gives

$$\boldsymbol{\varepsilon}_2(\boldsymbol{\xi}_2|m_1\mathbf{x}_0+\boldsymbol{\varepsilon}_1(\boldsymbol{\xi}_1|\mathbf{x}_0))\cong\boldsymbol{\varepsilon}_2(\boldsymbol{\xi}_2|m_1\mathbf{x}_0). \quad (16)$$

Since the ray aberration $\boldsymbol{\varepsilon}_1$ on the left-hand side of Eq. (16) produces only a higher than third-order term, it is neglected in the third-order aberration theory. Thus, Eq. (14) can be replaced by Eq. (15) under the third-order aberration theory, and this approximation plays an important role in the remainder of this paper.

The irradiance distribution in the second image plane is given by

$$E(\mathbf{x}_2)=E_p\iiint \mathrm{d}^2\mathbf{x}_0\mathrm{d}^2\mathbf{x}_1\mathrm{d}^2\boldsymbol{\xi}\left[\prod_{j=1}^{2}\frac{1}{z_j'^2}\delta\left(\frac{\mathbf{x}_j}{z_j'}-\frac{\mathbf{x}_{j-1}}{z_j}-\frac{\boldsymbol{\varepsilon}_j}{z_j'}\right)\right] \times E_0(\mathbf{x}_0), \quad (17)$$

where the pupil coordinate and object position dependency of $\boldsymbol{\varepsilon}_j(\boldsymbol{\xi}_j|\mathbf{x}_{j-1})$ is dropped for simplicity. Equation (17) can be written by

$$E(\mathbf{x}_2)=\iiint \mathrm{d}^2\mathbf{x}_1\mathrm{d}^2\mathbf{x}_1'\mathrm{d}^2\mathbf{x}_2'\left[\prod_{j=1}^{2}\frac{1}{z_j'^2}\delta\left(\frac{\mathbf{x}_j}{z_j'}-\frac{\mathbf{x}_{j-1}}{z_j}\right)\right] \times[G(\mathbf{x}_1,\mathbf{x}_2,\mathbf{x}_1',\mathbf{x}_2'|\mathbf{x}_{\mathrm{obj}})], \quad (18)$$

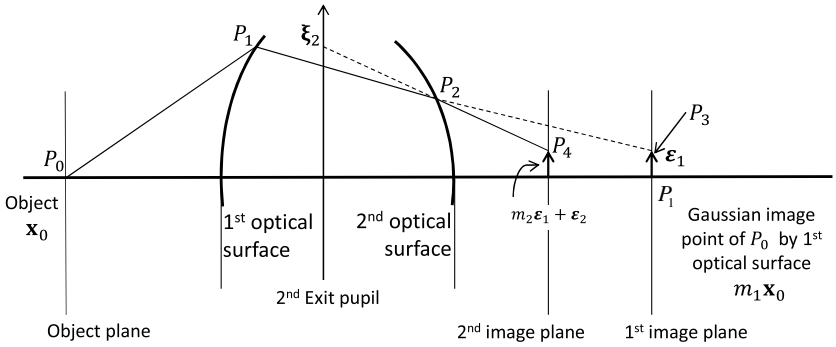

Fig. 3. Schematic layout of a two-surface optical imaging system.

where

$$G(\mathbf{x}_1,\mathbf{x}_2,\mathbf{x}'_1,\mathbf{x}'_2|\mathbf{x}_{\text{obj}}) = E_p \int \mathrm{d}^2\boldsymbol{\xi}\,\delta(\mathbf{x}_1-\mathbf{x}'_1-\varepsilon_1)\delta(\mathbf{x}_2-\mathbf{x}'_2-\varepsilon_2) \cong \delta(\mathbf{x}_1-\mathbf{x}'_1)\mathrm{PSF}_G(\mathbf{x}_2-\mathbf{x}'_2|\mathbf{x}_{\text{obj}}) \quad (19)$$

and Eq. (16) is used at the last step. The geometrical PSF is now given by

$$\mathrm{PSF}_G(\mathbf{x}_2|\mathbf{x}_{\text{obj}}) \cong E_p \int \mathrm{d}^2\boldsymbol{\xi}_2\,\delta(\mathbf{x}_2 + r_2\nabla_2 W(\boldsymbol{\xi}_2|\mathbf{x}_{\text{obj}})). \quad (20)$$

Substituting Eq. (19) into Eq. (18), the irradiance distribution function becomes

$$E(\mathbf{x}_2) \cong \mathrm{PSF}_G(\mathbf{x}_2|\mathbf{x}_{\text{obj}}) \otimes \delta(\mathbf{x}_2 - m_2 m_1 \mathbf{x}_{\text{obj}}), \quad (21)$$

which is a simple convolution of the geometrical PSF with a delta function centered on Gaussian image position.

D. Review of Imaging Equations for *n* Surfaces

Let us now consider an optical imaging system with n surfaces. The irradiance distribution function is

$$E(\mathbf{x}_n) = E_p \int \cdots \int \mathrm{d}^2\mathbf{x}_0 \cdots \mathrm{d}^2\mathbf{x}_{n-1}\mathrm{d}^2 \times \xi\left[\prod_{j=1}^{n} \frac{1}{z'^2_j}\delta\left(\frac{\mathbf{x}_j}{z'_j} - \frac{\mathbf{x}_{j-1}}{z_j} - \frac{\boldsymbol{\varepsilon}_j}{z'_j}\right)\right] E_0(\mathbf{x}_0). \quad (22)$$

Equation (22) can be written as

$$E(\mathbf{x}_n) = \int \ldots \int \mathrm{d}^2\mathbf{x}_0 \ldots \mathrm{d}^2\mathbf{x}_{n-1}\mathrm{d}^2\mathbf{x}'_1 \ldots \mathrm{d}^2\mathbf{x}'_n \times \left[\prod_{j=1}^{n} \frac{1}{z'^2_j}\delta\left(\frac{\mathbf{x}'_j}{z'_j} - \frac{\mathbf{x}_{j-1}}{z_j}\right)\right] \times [G(\mathbf{x}_1,\cdots,\mathbf{x}_n,\mathbf{x}'_1,\cdots,\mathbf{x}'_n|\mathbf{x}_0)]E_0(\mathbf{x}_0), \quad (23)$$

where

$$G(\mathbf{x}_1,\ldots,\mathbf{x}_n,\mathbf{x}'_1,\ldots,\mathbf{x}'_n|\mathbf{x}_0) = E_p \int \mathrm{d}^2\boldsymbol{\xi}\left[\prod_{j=1}^{n}\delta(\mathbf{x}_j - \mathbf{x}'_j - \boldsymbol{\varepsilon}_j)\right]. \quad (24)$$

Ignoring higher orders as shown in Eq. (16), the function G is simplified to

$$G(\mathbf{x}_1,\cdots,\mathbf{x}_n,\mathbf{x}'_1,\cdots,\mathbf{x}'_n|\mathbf{x}_0) \cong \left[\prod_{j=1}^{n-1}\delta(\mathbf{x}_j - \mathbf{x}'_j)\right]\mathrm{PSF}_G \times (\mathbf{x}_n - \mathbf{x}'_n|\mathbf{x}_0), \quad (25)$$

where the geometrical PSF is given by

$$\mathrm{PSF}_G(\mathbf{x}_n|\mathbf{x}_{\text{obj}}) = E_p \int \mathrm{d}^2\boldsymbol{\xi}_n\,\delta(\mathbf{x}_n + r_n\nabla_n W(\boldsymbol{\xi}_n|\mathbf{x}_{\text{obj}})). \quad (26)$$

Substituting Eq. (25) into Eq. (23), the image irradiance distribution function becomes

$$E(\mathbf{x}_n) = \mathrm{PSF}_G(\mathbf{x}_n|\mathbf{x}_{\text{obj}}) \otimes \delta(\mathbf{x}_n - m\mathbf{x}_{\text{obj}}). \quad (27)$$

Again, note that the exit pupil of the last surface coincides with the exit pupil of the total optical system.

3. Image Degradation Due to Surface Scatter Effects

For a given wavelength of light, the bidirectional scattering distribution function (BSDF) of a surface is defined as the scattering radiance divided by the incident irradiance [11]:

$$\mathrm{BSDF}(\boldsymbol{\alpha}_s,\boldsymbol{\alpha}_0) = \frac{dL_s(\boldsymbol{\alpha}_s,\boldsymbol{\alpha}_0)}{dE_i}, \quad (28)$$

where P_{inc} is the total radiant power illuminating a given surface area, $\boldsymbol{\alpha}_s$ is given by the direction cosines of a scattered ray multiplied by the index of refraction of the space, and $\boldsymbol{\alpha}_0$ is given by the direction cosines of the specular ray multiplied by the index of refraction. Note that, if $\boldsymbol{\alpha}_i$ is defined by the direction cosines of a incident ray multiplied by the index of refraction of the space, Snell's law becomes simply $\boldsymbol{\alpha}_i = \boldsymbol{\alpha}_0$. Assuming that the optical element has isotropic and homogeneous roughness over the whole surface and the BSDF is shift invariant relative to the incident angle for small incident and scattering angles, the BSDF can be written as

$$\mathrm{BSDF}(\boldsymbol{\alpha}_s - \boldsymbol{\alpha}_0) \cong Q \cdot [A \cdot \delta(\boldsymbol{\alpha}_s - \boldsymbol{\alpha}_0) + S(\boldsymbol{\alpha}_s - \boldsymbol{\alpha}_0)], \quad (29)$$

where Q is the reflectance (transmittance) of the surface, A is that fraction of the total reflected (transmitted) radiant power contained in the specular beam, and S is the incoherent scattering function [12]. The delta function corresponds to the specular light. Note that the BSDF contains both the specular and the scattered light; however, some authors ignore the specular beam when displaying BSDF plots. Because of reflection, transmission, or absorption losses, Q is generally less than unity; however, for the remainder of this paper, it is assumed that $Q = 1$.

A single scattered ray can be understood as a ray deviated from the specular direction, carrying the energy dictated by the BSDF. From the point of view of wavefront analysis, the angle of deviation from a certain reference direction can be expressed in terms of a wavefront error, which can be expressed as

$$W'(\mathbf{x}_0,\boldsymbol{\xi},\boldsymbol{\alpha}) = W(\mathbf{x}_0,\boldsymbol{\xi}) + W_s(\boldsymbol{\alpha},\boldsymbol{\xi}), \quad (30)$$

where W_s is the wavefront error of a scattered ray relative to the specular ray. Under the assumption of shift invariance of the BSDF, the wavefront error of a scattered ray is a linear function of the surface coordinates. Specifically, its mathematical form is the same as a wavefront tilt error

$$W'(\mathbf{x}_0, \boldsymbol{\xi}, \boldsymbol{\alpha}) = W(\mathbf{x}_0, \boldsymbol{\xi}) - \boldsymbol{\alpha} \cdot \boldsymbol{\xi}, \tag{31}$$

where n is index of refraction of image space. Using Eq. (31), the formalism developed in Section 2 will be used in a straightforward manner to analyze image degradation due to scattered light in the absence of aberrations.

A. Image Degradation Due to Surface Scatter in the Absence of Aberrations

Figure 4 shows a ray aberration due to scattering in the jth optical surface. Consider the aberration-free case, which is given by $\boldsymbol{\varepsilon}_j = 0$. Because of the position of the exit pupil, the "angle" $\boldsymbol{\alpha}'_j$ and the scattering "angle" $\boldsymbol{\alpha}_j$ may be different, and their geometrical relationship is given by $\boldsymbol{\alpha}_j = \boldsymbol{\alpha}'_j r_j / z'_j$. Using Eqs. (4), (8), and (31), the ray intercept position, $\mathbf{x}_j$, in the jth image plane for a scattered ray with a scattering angle $\boldsymbol{\alpha}_j$ is given by

$$\delta(\mathbf{x} - \mathbf{x}_j) = \delta\left(\mathbf{x} - \frac{z'_j}{z_j}\mathbf{x}_{j-1} - r_j \boldsymbol{\alpha}'_j\right). \tag{32}$$

The (fractional) infinitesimal power dP carried by a scattered ray bundle having $\boldsymbol{\alpha}_j$ is given by

$$dP = \mathrm{BSDF}_j(\boldsymbol{\alpha}_j) d\boldsymbol{\alpha}_j = \frac{r_j^2}{z_j'^2} \mathrm{BSDF}_j\left(\frac{r_j}{z'_j}\boldsymbol{\alpha}'_j\right) d\boldsymbol{\alpha}'_j. \tag{33}$$

The point source image irradiance distribution function for an aberration-free n-surface optical system with moderately rough surfaces can be expressed as

$$\begin{aligned} E(\mathbf{x}_n) &= P_{\mathrm{inc}} \int \cdots \int \mathrm{d}^2\mathbf{x}_0 \cdots \mathrm{d}^2\mathbf{x}_{n-1} \mathrm{d}^2\boldsymbol{\alpha}'_1 \cdots \mathrm{d}^2\boldsymbol{\alpha}'_j \prod_{j=1}^{n} \frac{r_j^2}{z_j'^2} \\ &\quad \times \mathrm{BSDF}_j\left(\frac{r_j}{z'_j}\boldsymbol{\alpha}'_j\right) \frac{1}{z_j'^2} \delta\left(\frac{\mathbf{x}_j}{z'_j} - \frac{\mathbf{x}_{j-1}}{z_j} - \frac{r_j}{z'_j}\boldsymbol{\alpha}'_j\right) E_0(\mathbf{x}_0) \\ &= P_{\mathrm{inc}} \int \cdots \int \mathrm{d}^2\mathbf{x}_0 \cdots \mathrm{d}^2\mathbf{x}_{n-1} \\ &\quad \times \left[\prod_{j=1}^{n} T_j(\mathbf{x}_j | \mathbf{x}_{j-1})\right] E_0(\mathbf{x}_0), \end{aligned} \tag{34}$$

where the intermediate kernel function T_j is defined by

$$\begin{aligned} T_j(\mathbf{x}_j | \mathbf{x}_{j-1}) &= \int \mathrm{d}^2\boldsymbol{\alpha}'_j \frac{r_j^2}{z_j'^2} \mathrm{BSDF}_j\left(\frac{r_j}{z'_j}\boldsymbol{\alpha}'_j\right) \frac{1}{z_j'^2} \delta\left(\frac{\mathbf{x}_j}{z'_j} - \frac{\mathbf{x}_{j-1}}{z_j} - \frac{r_j}{z'_j}\boldsymbol{\alpha}'_j\right) \\ &= \frac{1}{z_j'^2} \mathrm{BSDF}_j\left(\frac{\mathbf{x}_j}{z'_j} - \frac{\mathbf{x}_{j-1}}{z_j}\right). \end{aligned} \tag{35}$$

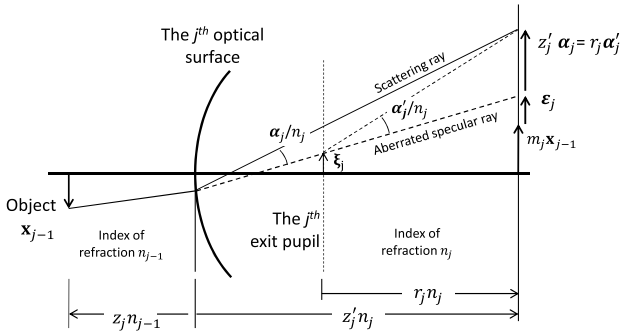

Fig. 4. Ray aberration due to scattering in a single surface.

Note that, within the small angle regime, the variable of the BSDF is

$$\frac{\mathbf{x}_j}{z'_j} - \frac{\mathbf{x}_{j-1}}{z_j} \cong \boldsymbol{\alpha}_s - \boldsymbol{\alpha}_0. \tag{36}$$

After some algebra, Eq. (34) reduces to the simpler form of

$$\begin{aligned} E(\mathbf{x}_n) &= P_{\mathrm{inc}} \frac{1}{d_n^2} \mathrm{BSDF}_n\left(\frac{\mathbf{x}_n}{d_n}\right) \otimes \cdots \otimes \frac{1}{d_1^2} \mathrm{BSDF}_1\left(\frac{\mathbf{x}_n}{d_1}\right) \\ &\quad \otimes \delta(\mathbf{x}_n - m\mathbf{x}_{\mathrm{obj}}) \equiv P_{\mathrm{inc}} \mathrm{PSF}_S(\mathbf{x}_n) \\ &\quad \otimes \delta(\mathbf{x}_n - m\mathbf{x}_{\mathrm{obj}}), \end{aligned} \tag{37}$$

where PSF_S stands for the PSF due to surface scatter as magnified by the imaging system. The magnified conjugate distance is given by $d_j = z' h_j / h$, where h_j is marginal ray height at the jth optical surface, h is the exit pupil height of the total optical system, and z' is image-side conjugate distance of the total optical system.

If it is assumed that only the jth surface is rough and all the other surfaces are perfectly smooth, Eq. (37) reduces to

$$\mathrm{PSF}_S(\mathbf{x}) = P_{\mathrm{inc}} \frac{1}{d_j^2} \mathrm{BSDF}_j\left(\frac{\mathbf{x}}{d_j}\right), \tag{38}$$

which is identical to Peterson's result [1,2].

B. Image Degradation Due to Surface Scatter in the Presence of Aberrations

The ray intercept position $\mathbf{x}_j$ in the jth image plane for a scattered ray with a scattering angle $\boldsymbol{\alpha}_j$ at the exit pupil position $\boldsymbol{\xi}_j$ at the jth exit pupil is

$$\delta(\mathbf{x} - \mathbf{x}_j) = \delta\left(\mathbf{x} - \frac{z'_j}{z_j}\mathbf{x}_{j-1} - r_j\boldsymbol{\alpha}'_j - \boldsymbol{\varepsilon}_j\right). \tag{39}$$

With the assumption that the exit pupil is uniformly illuminated, the image irradiance distribution function for a point source by an n-surface optical system is given by

$$E(\mathbf{x}_n) = \int \cdots \int \mathrm{d}^2\mathbf{x}_0 \ldots \mathrm{d}^2\mathbf{x}_{n-1} K(\mathbf{x}_0, \cdots, \mathbf{x}_n) E_0(\mathbf{x}_0), \tag{40}$$

where the kernel function K is

$$K = E_p \int \cdots \int \mathrm{d}^2\boldsymbol{\alpha}'_1 \cdots \mathrm{d}^2\boldsymbol{\alpha}'_n \mathrm{d}^2\boldsymbol{\xi} \times \left[\prod_{j=1}^{n} \frac{r_j^2}{z_j'^2} \mathrm{BSDF}_j\left(\frac{r_j}{z'_j}\boldsymbol{\alpha}'_j\right) \frac{1}{z_j'^2} \delta\left(\frac{\mathbf{x}_j}{z'_j} - \frac{\mathbf{x}_{j-1}}{z_j} - \frac{r_j\boldsymbol{\alpha}'_j}{z'_j} - \frac{\boldsymbol{\varepsilon}_j}{z'_j}\right) \right]. \tag{41}$$

If the value of $r_j\boldsymbol{\alpha}'_j$ is smaller than or similar to the value of $\boldsymbol{\varepsilon}_j$, the approximation in Eq. (16) can be extended to the case in the presence of both scattering and aberration by

$$\boldsymbol{\varepsilon}_{j+1}(\boldsymbol{\xi}_{j+1} | m_j\mathbf{x}_{j-1} + r_j\boldsymbol{\alpha}'_j + \boldsymbol{\varepsilon}_j) \cong \boldsymbol{\varepsilon}_{j+1}(\boldsymbol{\xi}_{j+1} | m_j\mathbf{x}_{j-1}), \tag{42}$$

which is discussed in detail in Subsection 3.C. Then the kernel function becomes simply

$$K = \int \cdots \int \mathrm{d}^2\mathbf{x}'_1 \cdots \mathrm{d}^2\mathbf{x}'_n \left[\prod_{j=1}^{n} T_j(\mathbf{x}_j | \mathbf{x}_{j-1}) \right] \times [G(\mathbf{x}_1, \cdots, \mathbf{x}_n, \mathbf{x}'_1, \cdots, \mathbf{x}'_n | \mathbf{x}_0)], \tag{43}$$

where the function T_j is defined in Eq. (35) and the function G is defined in Eq. (24). Substituting Eq. (43) into Eq. (40), the irradiance distribution function reduces to the simple form

$$E(\mathbf{x}_n) = \mathrm{PSF}_G(\mathbf{x}_n | \mathbf{x}_{\mathrm{obj}}) \otimes \mathrm{PSF}_S(\mathbf{x}_n) \otimes \delta(\mathbf{x}_n - m\mathbf{x}_{\mathrm{obj}}) \equiv \mathrm{PSF}(\mathbf{x}_n) \otimes \delta(\mathbf{x}_n - m\mathbf{x}_{\mathrm{obj}}), \tag{44}$$

where the geometrical PSF is given by Eq. (26) and the scattering PSF is given by Eq. (37). Equation (44) is a magnified version of the simple convolution of the geometrical PSF with the scattering PSF, which is the main conclusion of the paper. The scattering "effect" and geometrical aberration "effect" can be separately calculated; then their combined effect can be calculated (approximately) by their convolution.

C. Approximations and Assumptions

To obtain Eq. (44), mainly an assumption and an approximation were used. The assumption is that the BSDF is shift invariant with respect to incident angle for both small incident and small scattering angles. This is not true in general [12]. However, for smooth surfaces, the BSDF has been shown to be directly proportional to the surface power spectral density (PSD) function for small scattering and incident angles [12–16]. The above assumption is thus totally valid for smooth surfaces when $\cos\theta_i \cong \cos\theta_s \cong 1$. For moderately rough surfaces and arbitrary incident and scattering angles, which is our main interest, the assumption is not strictly true. To the best of our knowledge, there is no analytic form describing the BSDF for moderately rough surfaces with arbitrary incident and scattered angles. However, the generalized Harvey–Shack (GHS) surface scatter theory provides a numerical model that allows us to calculate BSDFs from surface metrology data (surface PSDs) for moderately rough surfaces with arbitrary incident and scattered angles [12,17]. Thus, perhaps the departure from shift-invariant behavior could be calculated numerically to determine the range of parameters over which the predicted image degradation is accurate to within some allowable error. Experimental validation is perhaps another possible alternative.

The approximation specified in Eq. (42) enables us to obtain the transverse ray aberration for a scattered ray having scattered angle $\boldsymbol{\alpha}_j$ at the jth optical surface and $\boldsymbol{\alpha}_j$ at the $(j+1)$th optical surface by

$$\varepsilon_{j+1}^{(T)} \cong m_{j+1}(\boldsymbol{\varepsilon}_j + z'_j\boldsymbol{\alpha}_j) + (\boldsymbol{\varepsilon}_{j+1} + z'_{j+1}\boldsymbol{\alpha}_{j+1}), \tag{45}$$

where $\boldsymbol{\varepsilon}_{j+1}^{(T)}$ is the total ray aberration in the presence of scattering and aberrations. $\boldsymbol{\varepsilon}_j$ is the ray aberration in the absence of scattering whose Gaussian reference sphere is centered on the Gaussian image point of the jth optical surface. If $\boldsymbol{\alpha}_j = 0$ and $\boldsymbol{\alpha}_{j+1} = 0$, then Eq. (45) becomes a third-order (scattering-free) transverse ray aberration. If $z'_j\boldsymbol{\alpha}_j \gg \boldsymbol{\varepsilon}_j$ (referred to as case 1), the approximation may not be considered to be valid because of higher-order contributions, which is ignored by Eq. (42). On the other hand, if $z'_j\boldsymbol{\alpha}_j < \boldsymbol{\varepsilon}_j$ or the order of the amount of $z'_j\boldsymbol{\alpha}_j$ is similar to the order of $\boldsymbol{\varepsilon}_j$ (referred to as case 2), it is natural to conclude that the approximation would be considered to be valid. Thus, some ray intersection positions at the $(j+1)$th image plane predicted by Eq. (45) corresponding to case 1 would not be correct, but some others corresponding to case 2 could be considered to be acceptable approximations. From experimental observations, well-polished optical surfaces have exponentially decaying BSDFs relative to the specular ray direction [12,15,16,18,19]. Thus, rays deviated far from the specular ray (case 1) carry an extremely small amount of radiant power compared to the power carried by a scattered ray near the specular direction (case 2). And a ray whose trajectory is predicted with a relatively large amount of error carries very small amount of energy, and a ray whose trajectory is predicted with a relatively small amount of error carries very large amount of energy. Thus, we consider the approximation expressed by Eq. (42) to be sufficiently valid for performing engineering calculations for state-of-the-art mirror surfaces.

4. Application of a Two-Mirror EUV Telescope

Equation (44) developed in the previous section (referred to hereafter as the convolution method) is tested by comparing its prediction to the prediction by commercial software. Specifically, the convolution method is applied to the two-mirror telescope, which

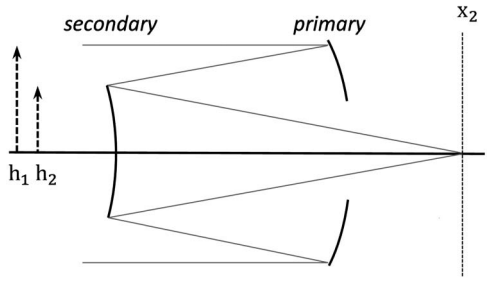

Fig. 5. Schematic layout of a Cassegrain-type two-mirror telescope. The marginal ray heights at the primary and secondary mirrors are designated by h_1 and h_2, respectively.

was considered in previous research [3]. Figure 5 illustrates the Cassegrain-type two-mirror telescope operating at EUV wavelengths. It has an effective focal length of 1750 mm, aperture diameter of 190 mm, and an obscuration ratio of 0.48. A mosaic detector array with 21 μm pixels is placed in the image plane. This telescope is intended to provide full solar disc images, over a field of view of $\pm 0.5°$. The telescope design is optimized to achieve similar geometrical spot sizes throughout the field of view. Its defocus and Seidel aberration coefficients (expressed in units of the wavelength) at a wavelength of 9.4 nm are shown in Table 1. In the previous work [3], aberrations were ignored, and only on-axis image quality was considered.

For the following analysis, it is assumed that the two mirror surfaces have the same isotropic and homogeneous statistical properties characterized by the surface metrology data from a state-of-the-art EUV telescope mirror. Four separate instruments were used to measure the optical fabrication errors of the mirror, and it is shown in Fig. 6. These measurements are consistent with the fact that most optical surfaces fabricated by conventional abrasive grinding and polishing techniques on ordinary amorphous glassy materials exhibit an inverse power-law surface PSD. The measured metrology data has thus been fit with a K-correlation function [3,12].

The BSDF of the mirror surfaces has been obtained from the fitted surface PSD function by using the GHS surface scatter theory, which has been shown to be valid for moderately rough surfaces and arbitrary incident and scattered angles [12]. The predicted BSDF profiles for three small incident angles are shown in Fig. 7. In Fig. 7(a), three predicted BSDF profiles are shown in direction cosine space, and the same profiles are shifted by the amount of specular direction in direction cosine space in Fig. 7(b). For small incident and scattering angles in this case, the predicted BSDF can thus be considered to be shift invariant.

Table 1. Defocus and Seidel Aberration Coefficients of the Two-Mirror Telescope ($\lambda = 9.4$ nm)

W_{020}	W_{040}	W_{131}	W_{222}	W_{220}	W_{311}
-30.35λ	0.42λ	-7.60λ	48.34λ	38.58λ	-5.48λ

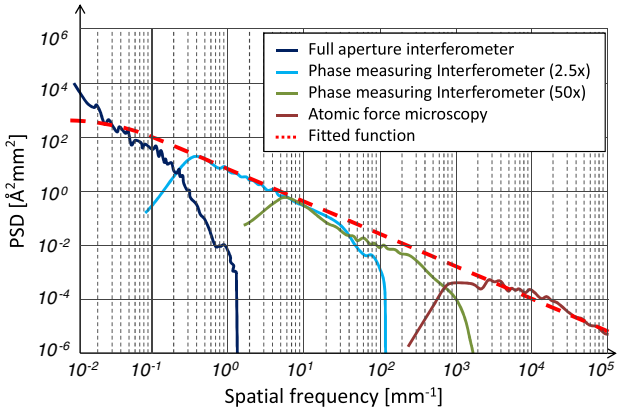

Fig. 6. (Color online) Composite surface PSD function determined from four different metrology instruments. A K-correlation function has been fit to the experimental data to characterize the surface.

At the wavelength of 9.4 nm, the total integrated scattering (TIS) for a single surface is equal to 0.56. Hence, for the two-mirror telescope, less than 19% of the radiant energy in the PSF resides in the specular beam; i.e., over 81% of the radiant energy is scattered [3]. At this wavelength, surface scatter is thus a very dominant image degradation mechanism.

The BSDF curves in Fig. 7(a) show exponentially decaying BSDFs, and its behavior is very close to shift invariant as shown in Fig. 7(b). These BSDF curves satisfy our two assumptions discussed in Subsection 3.C. To calculate the PSF using Eq. (44), the geometrical PSF and the scattering PSF are needed, and they can be separately obtained. The geometrical PSF is given by Eq. (26), but it is hard to calculate directly. Rather, the ray-tracing technique [8] or other methods [20] could be considered for practical reasons. And in this paper, a discrete sampling approach described in Appendix A is used to calculate the geometrical PSF. The scattering PSF can be obtained from Eq. (37). Here the optical system consists of two mirror surfaces, and the object is located at an infinite distance from the optical system, and the stop is located at the first surface; the magnified conjugate distances are given by $d_1 = f$, $d_2 = fh_2/h_1$, where f is the focal length of the entire system. Thus, the scattering PSF for the two-mirror telescope is given by

$$\mathrm{PSF}_S(\mathbf{x}) = \frac{1}{f^2(h_2/h_1)^2}\mathrm{BSDF}_2\left(\frac{\mathbf{x}}{fh_2/h_1}\right) \otimes \frac{1}{f^2}\mathrm{BSDF}_1\left(\frac{\mathbf{x}}{f}\right). \tag{46}$$

Because the BSDF may not be given by an analytic form, the two-dimensional convolution is calculated numerically {see [3] for details; note that symbol BSDF in [3] denotes the function S in Eq. (29) in this paper}.

The two-dimensional convolution of the geometrical PSF and scattering PSF is carried out numerically,

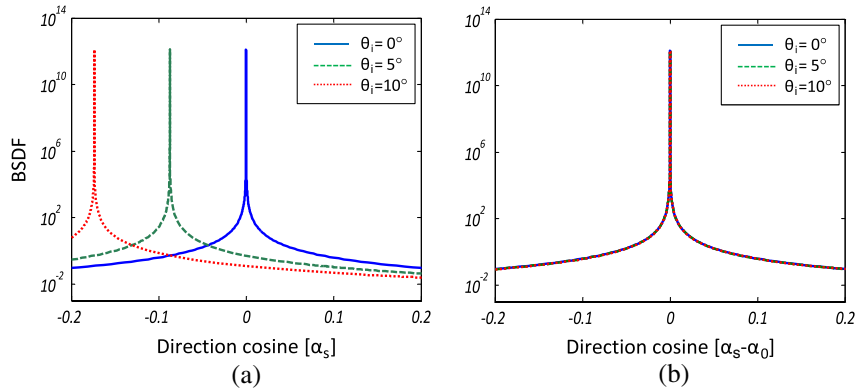

Fig. 7. (Color online) Predicted BSDF profiles for three small angles of incidence (θ_i) and small angle of scattering for 9.4 nm wavelength of light in (a) direction cosine space and (b) shifted direction cosine space.

and the resultant irradiance distribution (or PSF) is compared to the nonsequential ray-tracing results of one billion rays provided by the commercial software Zemax with a Monte Carlo technique [21–24]. In Fig. 8(a), a logarithmically scaled irradiance distribution in the image plane with size 4 × 4 detector pixels is predicted by the convolution method for a field angle of 0.5°. As a reference, the irradiance distribution predicted by Zemax is presented in Fig. 8(b). These irradiance distributions (or PSFs) are virtually indistinguishable by visual observations. In Figs. 8(c) and 8(d), the corresponding contour maps of the PSFs are shown. Again the two computational techniques produce virtually identical results, although the contour lines are somewhat smeared due to the Monte Carlo technique used in the nonsequential tracing of discrete rays. Note that the diameter of the Airy disk for full aperture at 9.4 nm wavelength is about 0.21 μm and the full width of a pixel is 21 μm.

In Figs. 9(a) and 9(b), the contour maps of logarithmically scaled irradiance distributions in an image plane with a size of 16 × 16 detector pixels for the

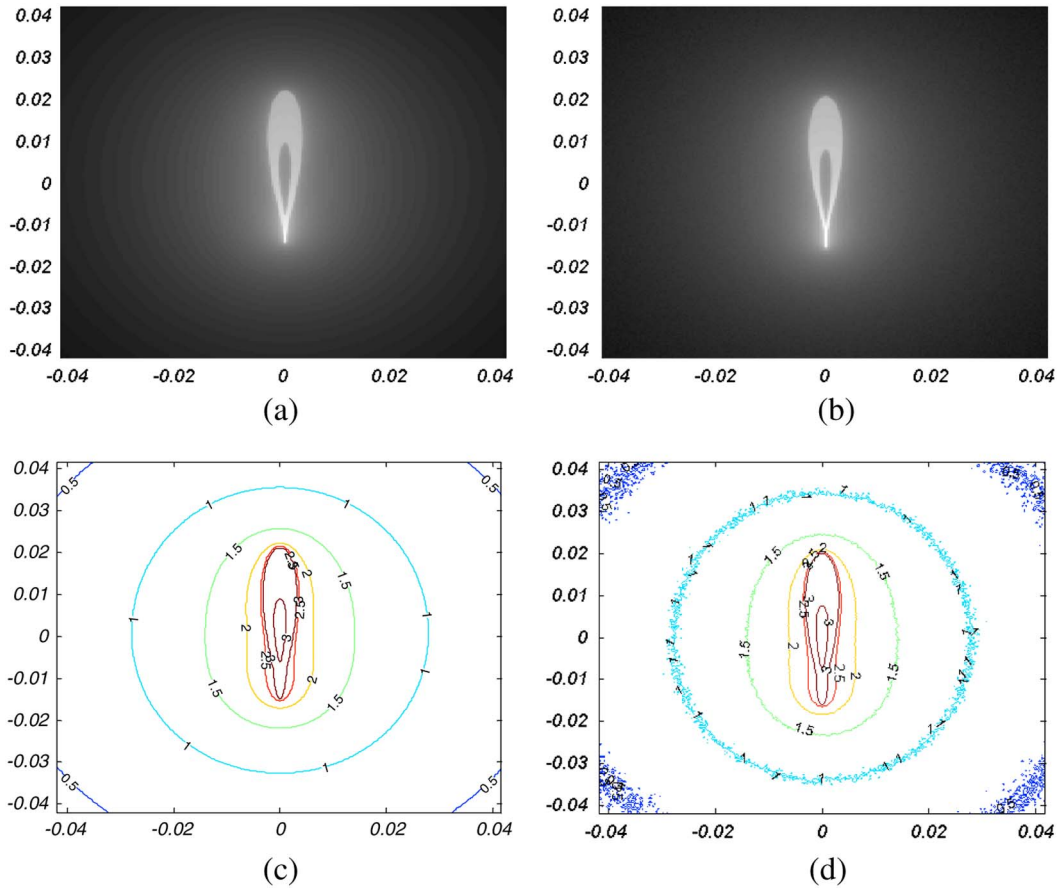

Fig. 8. (Color online) PSF by scattering and aberrations for 0.5° field angle by (a) the convolution method and (b) Zemax; (c) contour map of (a); (d) contour map of (b). Numbers in the axis denote axial distance from the Gaussian image point in millimeters.

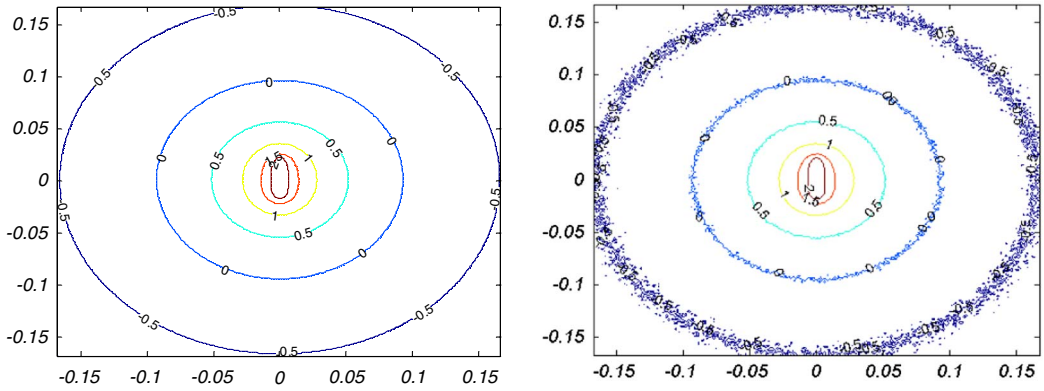

Fig. 9. (Color online) Illustration of the contour map of the composite PSF due to both scattering and aberrations for a 0.5° field angle as calculated by (a) the convolution method, (b) Zemax. Numbers in the axis denote axial distance from the Gaussian image point in millimeters.

same 0.5° field angle are predicted by the convolution method and by Zemax, respectively. This allows us to observe the irradiance contour lines of the predicted PSF at larger distances from the chief ray. The two computational techniques continue to provide almost indistinguishable results.

For estimating system performance, the fractional encircled energy is often used. However, in the case of an aberrated image, the PSF is no longer rotationally symmetric, and since square detector pixels are used, the energy contained in a square (referred to as en-squared energy) is chosen for evaluating system performance. The en-squared energy plots centered on the chief ray position for 0° field angle and 0.5° field angle are shown in Fig. 10, and the en-squared energy for the aberration-free case is also plotted (dotted line) as a reference. Since the dynamic range of the plot is over four decades and the number of sampling points is restricted, five en-squared energy plots for different sizes of the image plane are superimposed. Figure 10 shows excellent agreement between the convolution result (solid line) and Zemax result (asterisks). Furthermore, the en-squared energies for the two aberrated cases approach the en-squared energy of the aberration-free case for positions far from the Gaussian image position.

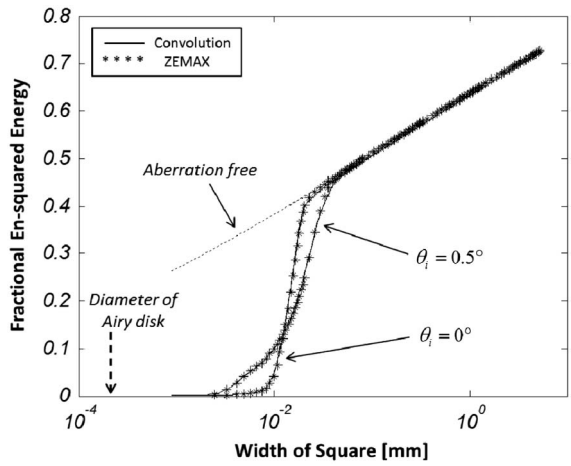

Fig. 10. En-squared energy for 0° and 0.5° field angle for the convolution method (solid line), Zemax (asterisks), and aberration-free case (dotted line) centered on the Gaussian image point.

Roughly speaking, aberrations are caused by macroscopic features (surface height deviations) from the ideal reference surface, and scattering is caused by microscopic features from the mean surface. Macroscopic (low spatial frequency) roughness contributes small angle ray deviations from the specular direction, and microscopic (high spatial frequency) roughness contributes large angle scattering from the specular direction. Thus, the existence of aberrations does not change the high-frequency scattering behavior as shown above in Fig. 8.

5. Summary and Conclusions

It is commonly believed that image degradation by surface scattering can be predicted only by nonsequential ray-tracing techniques, especially when aberrations are present in the optical system. We have developed a mathematical formulism showing that scattered light, under certain conditions, can be understood as an aberration and its effects on the system PSF can be easily evaluated by convolution of the scattering PSF_S with the geometrical PSF_G. By combining this knowledge with a generalization of Peterson's analytic approach to calculating the irradiance distribution in the focal plane of a multielement imaging system, we have demonstrated fast, accurate calculations of image quality for systems suffering from both surface scatter effects and conventional aberrations. And we have numerically validated that simple analytical approach to making image quality predictions with the computation-intensive calculations provided by the well-known Zemax code for an EUV telescope where image degradation due to surface scatter is substantial.

Appendix A

This Appendix is devoted to showing that the geometrical PSF given by Eq. (13), Eq. (21), or Eq. (26) is consistent with previous researchers' definition of the geometrical PSF [10,20] or ray intersection

density [25], or power density in image plane [8]. To avoid any "order"-related issue, let us assume that the relation between the transverse ray aberration $\boldsymbol{\varepsilon}(\boldsymbol{\xi})$ and the wave aberration $W(\boldsymbol{\xi})$ is given by

$$\boldsymbol{\varepsilon}(\boldsymbol{\xi}) = \mathsf{T}[W(\boldsymbol{\xi})], \tag{A1}$$

where the operator T is defined by $-r_j \nabla_j$ or an operator that gives exact ray aberration from the wave aberration. Figure 11(a) shows the pupil plane, and Fig. 11(b) shows the corresponding image plane. The shadowed infinitesimal region whose area is dS_p in Fig. 11(a) is mapped into the shadowed infinitesimal square whose area is dS_i centered on $\mathbf{x}_c$ in Fig. 11(b) by the operator T. Welford [25] states that the irradiance value at a given point in the image plane is proportional to the ratio of dS_p to dS_i, and Mahajan [10] shows that the explicit relation is

$$E(\mathbf{x}_c) = E_p \frac{dS_p}{dS_i}, \tag{A2}$$

where the ratio is obtained using the Jacobian determinant. Note that E_p is not constant in Mahajan's expression, but here we restrict our attention to the case of constant E_p. Meanwhile, Smith [8] uses the ray-tracing technique to describe the geometrical PSF. According to him, the geometrical PSF is obtained by uniformly discretizing of the pupil plane, obtaining the ray intersection position in the image plane by tracing each ray passing the discrete point, and counting the number of rays fallen on the given small area in the image plane.

In order to show the equivalence of the two approaches, consider a small region whose area ΔS_p in the pupil plane is mapped into small square whose area is ΔS_i (centered on $\mathbf{x}_c$) in the image plane by the operator T. Smith's statement can be expressed mathematically in the following steps. First, represent the position of the discrete sampling point in the pupil plane as $\boldsymbol{\xi}_m$, where m represents the mth sampling point out of the total N sampling points in the pupil. Second, trace each ray and obtain the ray intersection position in the image plane, which is represented by $\mathsf{T}[W(\boldsymbol{\xi}_m)]$. Third, introduce a function E that is a combination of delta functions

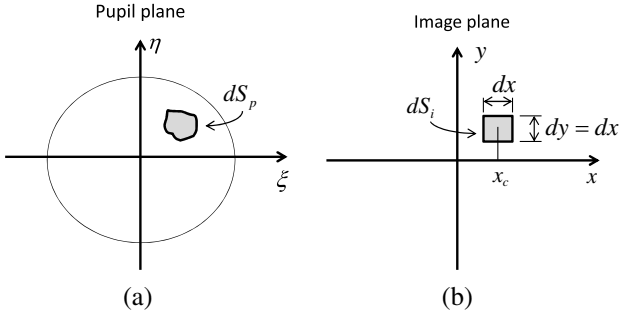

Fig. 11. Two infinitesimal areas in (a) pupil plane and (b) image plane. The infinitesimal area in (a) is mapped into infinitesimal square in (b).

centered on the ray intersection positions in the image plane:

$$E(\mathbf{x}) = E_p \frac{S_p}{N} \sum_{m=1}^{N} \delta(\mathbf{x} - \mathsf{T}[W(\boldsymbol{\xi}_m)]), \tag{A3}$$

where S_p is the total area of the pupil and $E_p S_p / N$ is the power that a ray is carrying. Last, take the average of the function $E(\mathbf{x})$ over the small square ΔS_i in the image plane, which is expressed by

$$\begin{aligned}
\mathsf{E}(\mathbf{x}_c) &= \frac{1}{\Delta S_i} \int_{\Delta S_i} \mathrm{d}^2\mathbf{x} E(\mathbf{x}) \\
&= E_p \frac{S_p}{N} \frac{1}{\Delta S_i} \int_{\Delta S_i} \mathrm{d}^2\mathbf{x} \sum_{m=1}^{N} \delta(\mathbf{x} - \mathsf{T}[W(\boldsymbol{\xi}_m)]) \\
&= E_p \frac{S_p}{N} \frac{1}{\Delta S_i} \int \mathrm{d}^2\mathbf{x} \sum_{m=1}^{M} \delta(\mathbf{x}) = E_p \frac{S_p}{N} \frac{1}{\Delta S_i} M \\
&= E_p \frac{1}{\Delta S_i} \left(S_p \frac{M}{N} \right),
\end{aligned} \tag{A4}$$

where M is the number of sampling points inside the ΔS_p in the pupil plane. Equation (A4) could be a mathematical illustration of Smith's method. If we take the limit of $N \to \infty$, the ratio of M/N approaches dS_p/S_p, and if we take the limit of $\Delta S_i \to 0$, the ratio of the two small areas becomes $\Delta S_p / \Delta S_i = dS_p / dS_i$. Thus, the value of E in those limits is given by

$$\lim_{\Delta S_i \to 0} \left(\lim_{N \to \infty} \mathsf{E} \right) = \lim_{\Delta S_i \to 0} \left(E_p \frac{\Delta S_p}{\Delta S_i} \right) = E_p \frac{dS_p}{dS_i}, \tag{A5}$$

which is an identical expression to Eq. (A2) when that number of sampling points in the pupil plane is large. Note that the physical dimension of $E(\mathbf{x})$ in Eq. (A3) is the radiant power times the physical dimension of the delta function.

In order to extend the mathematical illustration for discrete $\boldsymbol{\xi}_m$ to that for continuous a variable $\boldsymbol{\xi}$, define a rectangular parallelepiped function $\tau(x)$ by

$$\begin{aligned}
\tau(\mathbf{x}) &= \lim_{\Delta S_i \to 0} \frac{1}{\Delta S_i}, \quad -\tfrac{\Delta x}{2} < x < \tfrac{\Delta x}{2}, -\tfrac{\Delta x}{2} < y < \tfrac{\Delta x}{2}, \\
&= 0, \qquad\qquad \text{elsewhere},
\end{aligned} \tag{A6}$$

where $\Delta S_i = (\Delta x)^2$ and the physical dimension of the rectangular parallelepiped function is the inverse of area. Using the rectangular parallelepiped function, let us redefine the function $E(\mathbf{x})$:

$$E(x) = E_p \int \mathrm{d}^2\boldsymbol{\xi} \tau(\mathbf{x} - \mathsf{T}[W(\boldsymbol{\xi})]). \tag{A7}$$

Note that $\boldsymbol{\xi}$ is a continuous variable in the pupil plane. For the case of $\mathbf{x} = \mathbf{x}_c$, if the position given by the mapping operator $\mathsf{T}[W(\boldsymbol{\xi})]$ is inside of the shadowed square in Fig. 11(b), the integrand in Eq. (A7)

becomes a constant value of $1/\Delta S_i$. If $\mathsf{T}[W(\boldsymbol{\xi})]$ is outside of the square, the integrand becomes zero. Thus, the Eq. (A7) is reduced to

$$E(\mathbf{x}_c) = \lim_{\Delta S_i \to 0} E_p \int_{\Delta S_p} \mathrm{d}^2\boldsymbol{\xi} \frac{1}{\Delta S_i} = \lim_{\Delta S_i \to 0} E_p \frac{\Delta S_p}{\Delta S_i}$$
$$= E_p \frac{dS_p}{dS_i}, \tag{A8}$$

which is identical to Eq. (A4). The physical dimension of $E(\mathbf{x})$ in Eq. (A6) is irradiance, and, by definition, it can be called the geometrical PSF. Note that Eqs. (13), (21), and (26) have the same form as Eq. (A6) except delta function is used instead of $\tau(x)$.

Equation (A7) is not a good form for practical calculations, thus the geometrical PSF in Section 4 is calculated by following Smith's statement.

This work has been supported by the Lockheed Martin Solar and Astrophysical Laboratory (LMSAL) under Lockheed Martin Space Systems Subcontract number 8100001649 relating to the Solar Ultraviolet Imager (SUVI) for the GOES-R Satellite Series.

References

1. G. L. Peterson, "Analytic expressions for in-field stray light irradiance in imaging systems," Master's report (University of Arizona, 2003).
2. G. L. Peterson, "Analytic expressions for in-field scattered light distribution," Proc. SPIE **5178**, 184–193 (2004).
3. J. E. Harvey, N. Choi, A. Krywonos, G. Peterson, and M. Bruner, "Image degradation due to scattering effects in two-mirror telescopes," Opt. Eng. **49**, 063202 (2010).
4. J. W. Goodman, *Introduction to Fourier Optics*, 2nd ed. (McGraw-Hill, 1996).
5. J. E. Harvey and A. Krywonos, "A systems engineering analysis of image quality," Proc. SPIE **4093**, 379–388 (2000).
6. J. E. Harvey, A. Krywonos, M. Atanassova, and P. L. Thompson, "The Solar X-ray Imager (SXI) on GOES-13: design, analysis, and on-orbit performance," Proc. SPIE **6689**, 66890I (2007).
7. J. E. Harvey, M. Atanassova, and A. Krywonos, "Systems engineering analysis of five "as-manufactured" SXI telescopes," Proc. SPIE **5867**, 58670F (2005).
8. W. J. Smith, *Modern Optical Engineering*, 3rd and international ed. (McGraw-Hill, 2000), pp. 360–361, 372.
9. G. B. Arfken and H. J. Weber, *Mathematical Methods for Physicists*, 5th ed. (Academic, 2001).
10. V. N. Mahajan, *Optical Imaging and Aberrations: Part I* (SPIE, 1998), pp. 206–208, 281–287.
11. F. E. Nicodemus, "Reflectance nomenclature and directional reflectance and emissivity," Appl. Opt. **9**, 1474–1475 (1970).
12. A. Krywonos, J. E. Harvey, and N. Choi, "Linear systems formulation of scattering theory for rough surfaces with arbitrary incident and scattering angles," J. Opt. Soc. Am. A **28**, 1121–1138 (2011).
13. J. E. Harvey, "Light-scattering characteristics of optical surfaces," Ph.D. dissertation (University of Arizona, 1976).
14. J. E. Harvey, "Surface scatter phenomena: a linear, shift-invariant process," Proc. SPIE **1165**, 87–99 (1989).
15. P. Beckmann and A. Spizzichino, *The Scattering of Electromagnetic Waves from Rough Surfaces* (Pergamon, 1963).
16. J. C. Stover, *Optical Scattering, Measurement and Analysis*, 2nd ed. (SPIE, 1995).
17. J. E. Harvey, N. Choi, A. Krywonos, and J. Marcen, "Calculating BRDFs from surface PSDs for moderately rough surfaces," Proc. SPIE **7426**, 64260I (2009).
18. E. L. Church, "Fractal surface finish," Appl. Opt. **27**, 1518–1526 (1988).
19. R. J. Noll and P. Glenn, "Mirror surface autocovariance functions and their associated visible scattering," Appl. Opt. **21**, 1824–1838 (1982).
20. C. Liu and P. D. Lin, "Computational method for deriving the geometric point spread function of an optical system," Appl. Opt. **49**, 126–136 (2010).
21. *Zemax Development Corporation, Zemax User Manual, 3001 112th Avenue NE, Suite 202, Bellevue, Washington 98004-8017, USA (2009).*
22. N. Coluccelli, "Nonsequential modeling of laser diode stacks using Zemax: simulation, optimization, and experimental validation," Appl. Opt. **49**, 4237–4245 (2010).
23. Y. Luo, J. Castro, J. K. Barton, R. K. Kostuk, and G. Barbastathis, "Simulations and experiments of aperiodic and multiplexed gratings in volume holographic imaging systems," Opt. Express **18**, 19273–19285 (2010).
24. M. N. Akram, "Simulation and control of narcissus phenomenon using nonsequential ray tracing. II. Line-scan camera in 7–11 μm waveband," Appl. Opt. **49**, 1185–1195 (2010).
25. W. T. Welford, *Aberrations of Optical Systems* (Hilger, 1991), pp. 113–114.